Int. J. Electrochem. Sci., 16 **(2021)** Article ID: 210511, doi: 10.20964/2021.05.10

International Journal of
ELECTROCHEMICAL
SCIENCE
www.electrochemsci.org

Effects of CeO_2 on Microstructural Evolution, Corrosion and Tribology Behavior of Laser Cladded TiC Reinforced Co-based Coatings

Jianguo Chen[1], *Qiushi Li*[2,3,4,*], *Bing Sun*[5], *Qiuhong Zhao*[1], *Zejun Wang*[1], *Weifei Niu*[1], *Xuan Wang*[1,**], *Lihua Dang*[1], *Qingjun Ma*[1]

[1] Tianjin Special Equipment Inspection Institute, Tianjin 300192, PR China
[2] CCCC Tianjin Port Engineering Institute Co., Ltd., Tianjin 300222, P R China
[3] Tianjin Key Laboratory of Underwater Tunnel Construction and Operation & Maintenance Technology, Tianjin 300222, P R China
[4] CCCC First Harbor Engineering Co., Ltd., Tianjin 300461, P R China
[5] CenerTech Oil Production & Service Company, Tianjin, 300452, P R China
[*]E-mail: qsli@tju.edu.cn (Qiushi Li), [**]E-mail: 13802123211@126.com (Xuan Wang)

Received: 17 December 2020 / *Accepted:* 8 February 2021 / *Published:* 31 March 2021

TiC/Co-based composite coatings with different CeO_2 contents were successfully fabricated on 9Cr ferritic steel by laser cladding. The effects of CeO_2 on microstructure, corrosion and wear resistance of laser cladded TiC/Co-based composite coatings were investigated systemically. X-ray diffractometer (XRD) results showed that the coating layers consisted of four types of intermetallic phases, γ-Co, TiC, $TiWC_2$ and $Cr_{23}C_6$. TiC and $TiWC_2$ precipitates played a significant role in the corrosion and wear resistance of the cladding layer. Energy dispersive spectrometer (EDS) analyses indicated that the TiC is coated by the $TiWC_2$. The rare earth oxides could act as the nucleation positions for precipitates. Furthermore, the morphology and distribution of precipitates were significantly affected by CeO_2 additions. The corrosion resistance, micro-hardness, and wear resistance of the composite coatings increased first and then decreased as CeO_2 content increased. Appropriate addition of CeO_2 (1.5 wt.%) could lead to the refinement and uniform distribution of precipitates, resulting in the improvement of the corrosion resistance, hardness, and wear resistance. Excessive addition of CeO_2 could cause the accumulation of some precipitates, resulting in the uneven distribution of precipitates again, thereby reducing the corrosion resistance, hardness, and wear resistance of the cladding layer.

Keywords: TiC/Co-based composite coating, CeO_2, Microstructure, Corrosion resistance, Wear resistance

1. INTRODUCTION

Laser cladding is a surface engineering technology by depositing cladding materials on the surface of substrates under the action of high energy laser. It has become a promising technology in the

field of surface engineering, owing to the advantages in excellent wear resistance, corrosion resistance and oxidation resistance [1-3]. Fe-based, Ni-based, and Co-based powders are the most commonly used cladding materials. Guo et al. [4] fabricated a Fe-based coating with nano-scale bainitic microstructure using laser cladding, and found that the nano-structured bainitic ferrite and carbon-enriched retained austenite were distributed uniformly in the coating. Verdi et al. [5] reported that the laser cladded Inconel 625 coatings exhibited higher adhesion to the substrate, and the coatings improved the superficial hardness of the specimens. Zhao et al. [6] studied the microstructure and mechanical properties of Co-based alloy coatings fabricated by laser cladding, the micro-hardness of the laser cladding coatings was up to 1200 $HV_{0.2}$, and the high-temperature wear resistance was also excellent. Although laser cladding is an effective way to improve the quality of component surface, it is difficult to avoid the formation of defects such as cracking and holes [7]. Thus, the application of laser cladding in some special fields is still restricted.

Rare earth elements have significant impacts on cladding layers, which can refine the microstructure, improve the properties, and reduce the cracking sensitivity of coatings [8,9]. Sharma et al. found that La_2O_3 could refine the microstructure of Ni-based alloy cladding layer, and improve the wear resistance [10]. Ding et al. [11] reported CeO_2 could result in the formation of fine dendrite and equiaxed grains in Co-based coating, and increase the hardness and wear resistance. Recently, ceramic metal composite coatings have attracted considerable attention because of their better thermal stability, wear resistance, erosion resistance, good oxidation resistance and mechanical properties compared to metal cladding layers [12-15]. Li et al. [16] proved that WC could improve the hardness and abrasive resistance of laser cladding coatings. Savalani et al. [17] found that the TiC/Ti-based laser cladding composite coatings possessed high micro-hardness and excellent wear resistance. Cai et al. [18] investigated the effect of TiC/Al_2O_3 composite ceramic on laser cladding Ni60 coatings. The results indicated that the ceramic particles significantly improved the wear resistance of the coating, while excessive ceramic particles addition could result in the information of cracks in the coating. Up to now, the effect of rare earth elements on the metal cladding coatings has been widely investigated. However, the effect of rare earth elements on the ceramic metal composite coatings remains to be further explored.

This work is aimed to investigate the effect of CeO_2 on microstructure, corrosion resistance, hardness, and wear properties of laser cladded TiC/Co-based composite coatings. The results can provide guidance for the application of rare earth in laser cladded ceramic metal composite coatings.

2. MATERIALS AND EXPERIMENT METHODS

2.1 Sample Preparation

9Cr ferritic steel samples with dimensions of 80×50×10 mm^3 were used as a substrate during laser cladding process, and the chemical compositions are shown in Table 1. Stellite 6, a Co-based alloy powder, was selected as the laser cladding material. A certain amount of TiC particles was added into Stellite 6 powder as the strengthening phase (the weight ratio between TiC and Stellite 6 was 1:9). Table 2 presents the chemical compositions of Stellite 6, and the purity of the powder is higher than

99.5%. In addition, CeO_2 was added into the mixed powder composed of Stellite 6 and TiC with different amounts of 0 wt.%, 0.5 wt.%, 1.5 wt.%, and 3 wt.%, which were marked as 1#, 2#, 3# and 4#, respectively. The morphology and X-ray diffractometer (XRD) pattern of the original powders are shown in Figure 1. The specific proportion of the complete laser cladding powder is shown in Table 3. Finally, the cladding powders were mixed uniformly.

Table 1. Chemical compositions of the 9Cr ferritic steel in wt.%

C	Cr	W	Mo	Mn	Si	V	Nb	Fe
0.1	8.93	1.5	0.94	0.44	0.3	0.22	0.07	Bal.

Table 2. Nominal chemical compositions of Co-based alloy powder in wt.%

C	Cr	W	Ni	Fe	Mo	Si	Co
1.0	29.7	4.8	2.5	2.0	1.0	0.8	Bal.

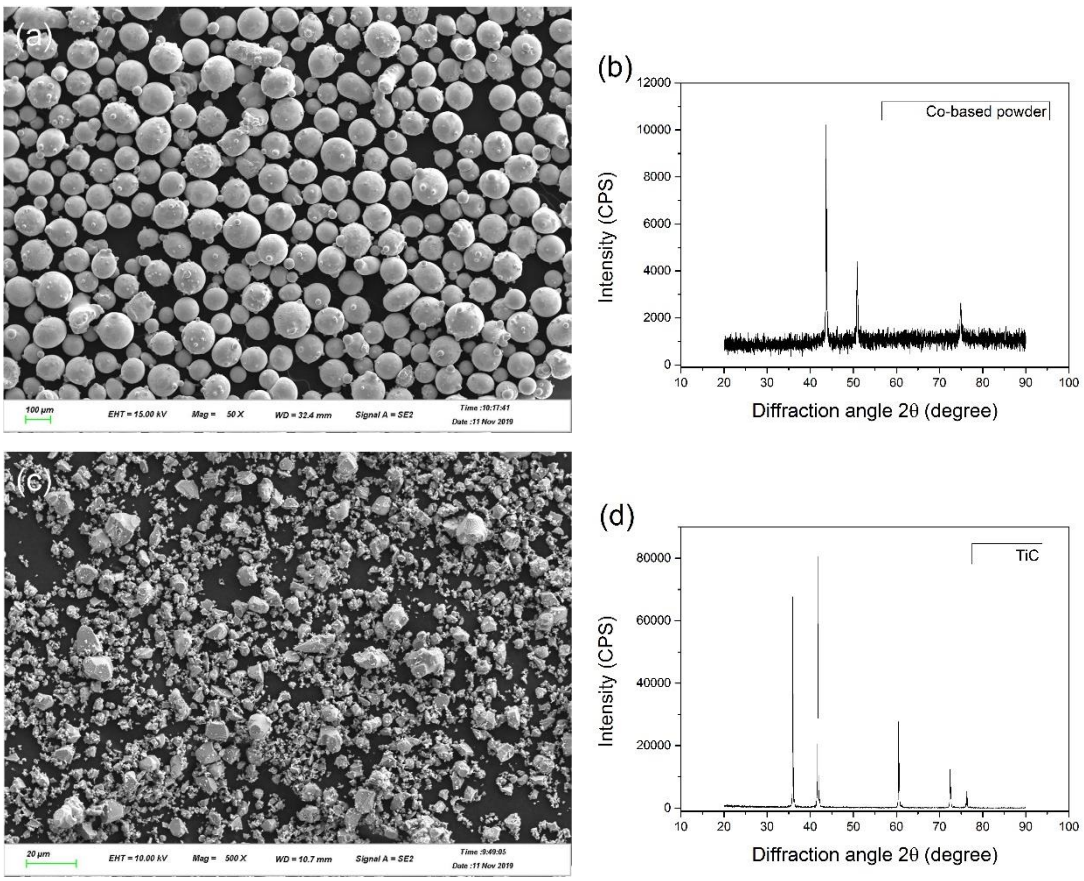

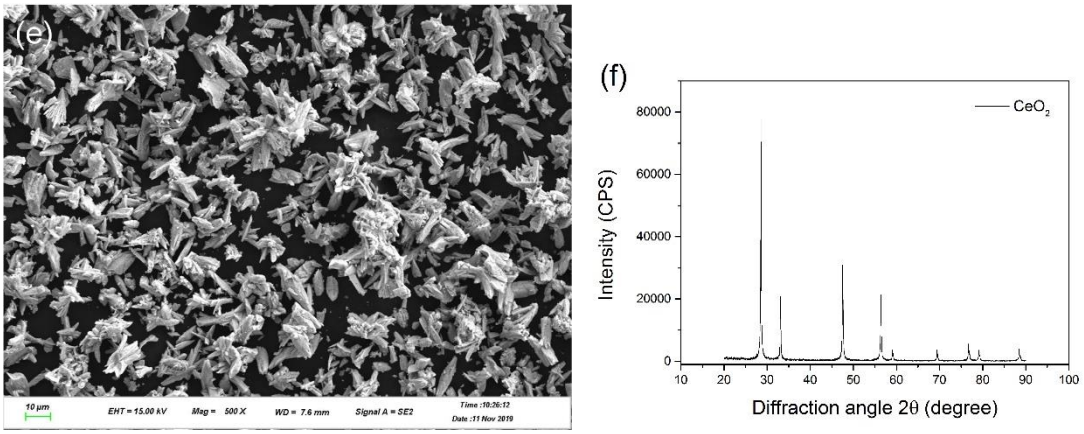

Figure 1. SEM morphologies (a, c, e) and XRD analysis (b, d, f) of original powders: (a) and (b) Co-based alloy powder, (c) and (d) TiC powder, (e) and (f) CeO_2 powder

Table 3. Chemical compositions of cladding layer powders in wt.%

Group	CeO_2	TiC+Stellite 6 (Ratio:1/9)
1#	0	100
2#	0.5	99.5
3#	1.5	98.5
4#	3	97

The schematic diagram of laser cladding is presented in Fig. 2. Before the laser cladding, substrates were ground by a series of SiC papers, followed by an ultrasonic cleaning with acetone and alcohol. After that, the cladding powders were mixed with alcohol and the concentration of the powders was similar to the cream. Finally, the cladding powders were coated on the surface of the substrate by laser. The JK2003SM type Nd: YAG laser equipment was used to prepare the cladding layer, and the laser cladding parameters are shown in Table 4.

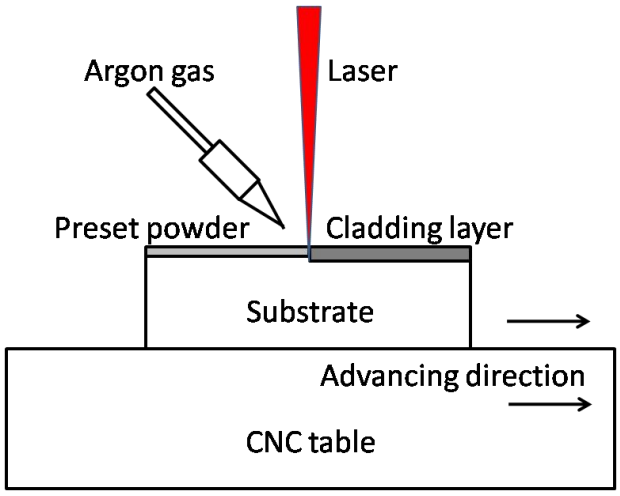

Figure 2. Schematic diagram of laser cladding

Table 4. Laser cladding parameters

Laser output power (W)	1600
Laser beam scanning velocity (mm/min)	180
Laser beam diameter (mm)	0.8
Argon flow rate (mL/min)	20
Overlap ratio (%)	30

2.2 Microstructure analysis

The samples after the laser cladding experiments were cut from the transversal cross-sections of the coating. The phase constitution in coatings was identified by XRD. The evolution of microstructure was investigated using optical microscope (OM) and scanning electron microscope (SEM). The worn surface of the composite coating was also studied by SEM.

2.3 Electrochemical measurements

The corrosion behaviors of the coatings were investigated using electrochemical impedance spectroscopy (EIS) by an Autolab 302N electrochemical workstation. The EIS measurements were conducted with a three-electrode system. The encapsulated specimens were used as working electrode with an exposed area of 1 cm^2. A platinum plate was used as counter electrode and an Ag/AgCl electrode (saturated with KCl) was served as reference electrode. The electrolyte solution used in the measurements was 3.5 wt.% NaCl solution at room temperature. EIS measurements were carried out at the open circuit potential with the frequency from 10^5 Hz to 0.01 Hz. The amplitude was set as 10 mV.

2.4 Micro-hardness and wear resistance measurements

The micro-hardness distribution of the coatings was measured using an MHV2000 type digital micro-hardness tester with a 100 g load and 10 s dwell. The wear resistance tests were carried out on an MM-200 dry sliding wear tester with a rotate rate of 200 r/min and a load of 49 N for 120min. The size of wear test specimens was 25×7×7 mm.

3. RESULTS AND DISCUSSION

3.1 Phase identification of TiC/Co-based composite coatings

Fig.3 shows the XRD spectra of laser cladded TiC/Co-based composite coatings with different CeO_2 contents. It can be found that the all the TiC/Co-based coatings are composed of the same solid solutions and hard particles phases, γ-Co, TiC, $TiWC_2$ and $Cr_{23}C_6$. The phase composition of cladding layers was independent upon the CeO_2 contents, and no CeO_2 or new phases containing cerium were observed with the addition of CeO_2, which could be explained by the small amount of CeO_2 addition [19]. γ-Co is a high-temperature phase retained in the cladding layers due to rapid cooling. High levels

of Cr and W in Co-based alloy power, combined with the decomposition product of original TiC particles under the action of laser, lead to the formation of TiC, $TiWC_2$ and $Cr_{23}C_6$.

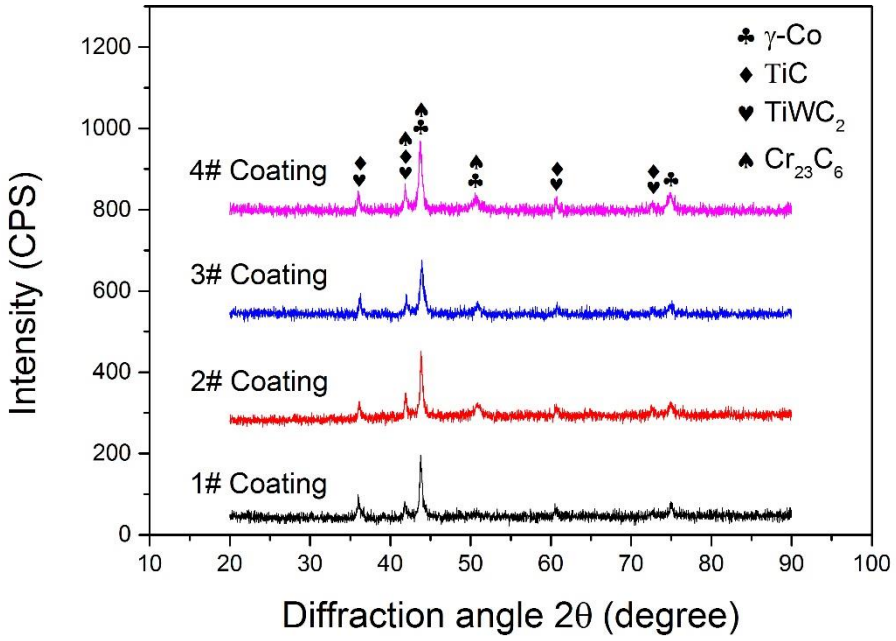

Figure 3. XRD patterns of TiC/Co-based composite coatings with different CeO_2 contents

3.2 Microstructure characteristics of TiC/Co-based composite coatings

Fig.4 shows the microstructure of TiC/Co-based composite coatings with different CeO_2 contents. The microstructure adjacent to the top surface exhibits equiaxed grains, as shown in Fig. 4(a), Fig. 4(c), Fig. 4(e) and Fig. 4(g). The columnar grains appear at the bonding interface, as shown in Fig. 4(b), Fig. 4(d), Fig. 4(f) and Fig. 4(h). The forming of grains with different morphologies in the cladding layer is related to the heat dissipation effect. At the bonding interface, G (temperature gradient) is large enough, R (solidification rate) tends to 0, and the G/R ratio tends to infinity. Columnar grains are obtained due to the highest speed of heat dissipation along the normal direction of the substrate. The cooling rate decreases significantly as the substrate temperature increases, and the G/R value decreases as the temperature gradient drops. The heat dissipation speed decreases at the later stage of molten pool solidification. The G/R value becomes smaller with the decrease of G and the increase of R [20,21]. Furthermore, the impurities existed on the surface of the molten pool can act as nucleation sites under the strong stir effect of laser. As a result, the grains close to the top of the cladding layer exhibit equiaxed.

As shown in Fig. 4(a) and Fig. 4(b), the size and distribution of precipitated particles are extremely uneven when the CeO_2 content was 0 wt.%. The size of precipitates varies greatly, and the precipitates exhibit irregular shapes and a certain degree of aggregation. With the increase of CeO_2 content, the precipitates are gradually distributed homogeneously on the matrix metal, and the size tends to be uniform, as shown in Fig. 4(c), Fig. 4(d), Fig. 4(e) and Fig. 4(f). The morphology of the hard precipitated particles change from dendrites to particles as the CeO_2 content increases from 0

wt.% to 0.5 wt.% and 1.5 wt.%. However, the precipitated particles are aggregated, as circled in Fig. 4(g) and Fig. 4(h), and the distribution becomes uneven again when the CeO_2 content increases to 3 wt.%. The excessive addition of rare earth element can lose the spheroidisation and refinement effects on the hard precipitated particles [22]. Besides, the grain coarsening was also observed, as shown in Fig. 4(g) and Fig. 4(h). The grain boundaries are polluted by the excessive rare earth element addition, and weakens the restriction to the grain growth [21].

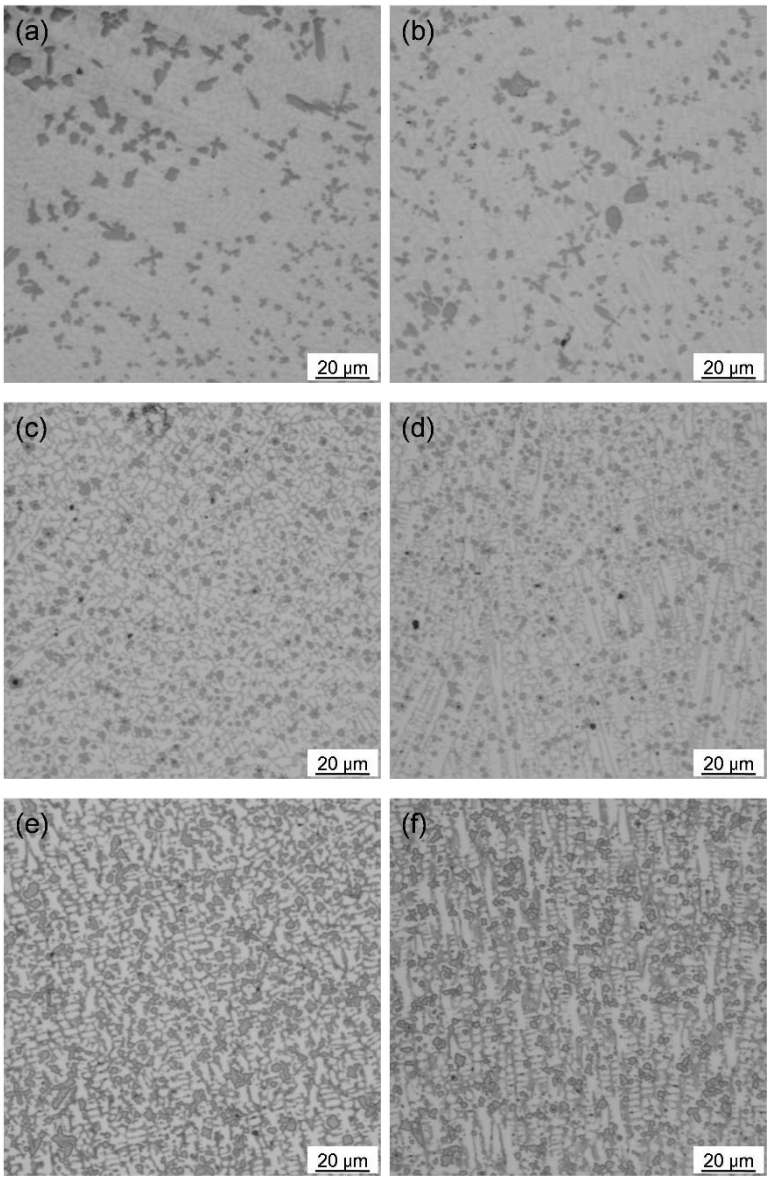

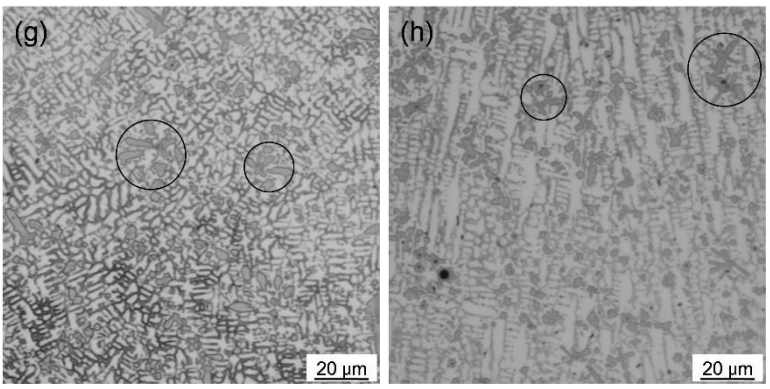

Figure 4. Microstructure of TiC/Co-based composite coatings: (a) and (b) 0 wt.% CeO_2, (c) and (d) 0.5 wt.% CeO_2, (e) and (f) 1.5% wt.% CeO_2, (g) and (h) 3% wt.% CeO_2

Fig. 5 and Fig. 6 show the energy dispersive spectrometer (EDS) analyses of the precipitated particles morphology and element distribution in laser cladded TiC/Co-based composite coatings with and without CeO_2 additions, respectively. The elemental segregation is clearly revealed in the EDS mapping results. Although the area of W, Ti and C in EDS mapping analyses is almost the same, the content of W and Ti is obviously different in dark grey and light grey areas of SEM images, as shown by EDS mapping analyses and point analyses in Fig. 5 and Fig. 6. By EDS and XRD analyses, it can be determined that the cladding layers consist of γ-Co, reticulated eutectic carbide $Cr_{23}C_6$, TiC and $TiWC_2$ precipitated particles regardless of the CeO_2, and TiC is coated by the $TiWC_2$. TiC powder has higher absorption of laserenergy [23]. Original TiC particles are decomposed into Ti and C by high energy laser beam, interacting with W in the Co-based alloy powder to form TiC and $TiWC_2$ precipitated particles, and C combined with Cr in the Co-based alloy powder to form $Cr_{23}C_6$, which is consistent with the XRD result in Fig. 3. Comparing Fig. 5 and Fig. 6, it can be clearly found that the morphologies of the TiC and $TiWC_2$ particles are different. The TiC and $TiWC_2$ precipitates in Fig.5 are aggregated, while the TiC and $TiWC_2$ in Fig.6 are individually nucleated. TiC and $TiWC_2$ precipitated particles with CeO_2 addition are finer, as shown in Fig. 6, Fig. 4(c), Fig. 4(d), Fig. 4(e) and Fig. 4(f).

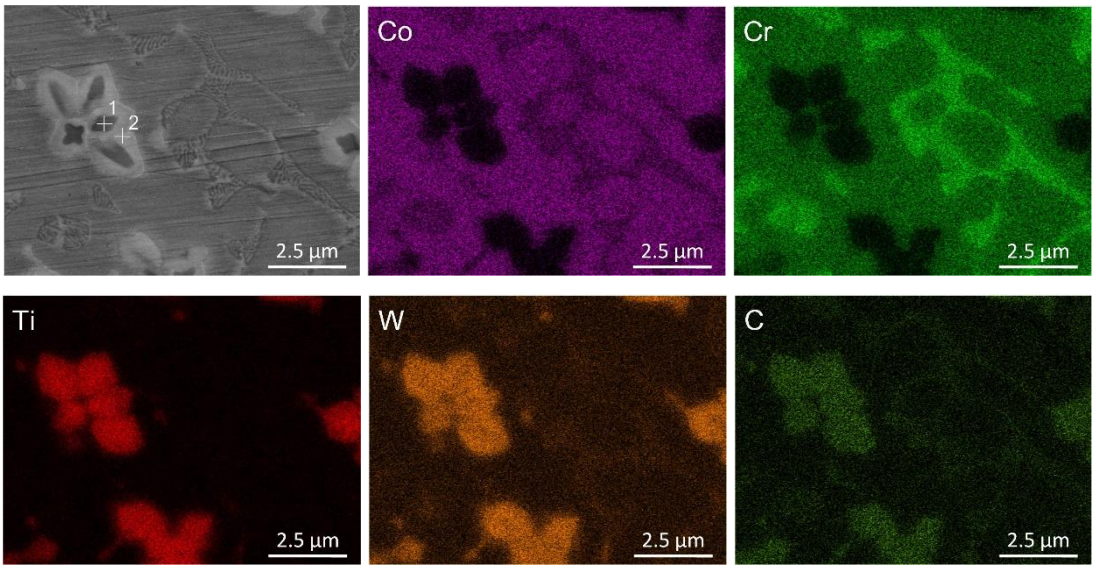

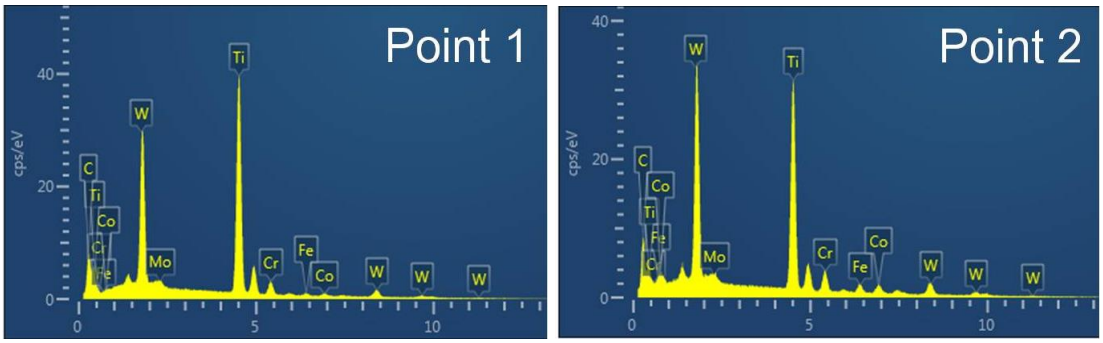

Figure 5. EDS analyses of the precipitated particles morphology and element distribution in TiC/Co-based composite coating without CeO_2

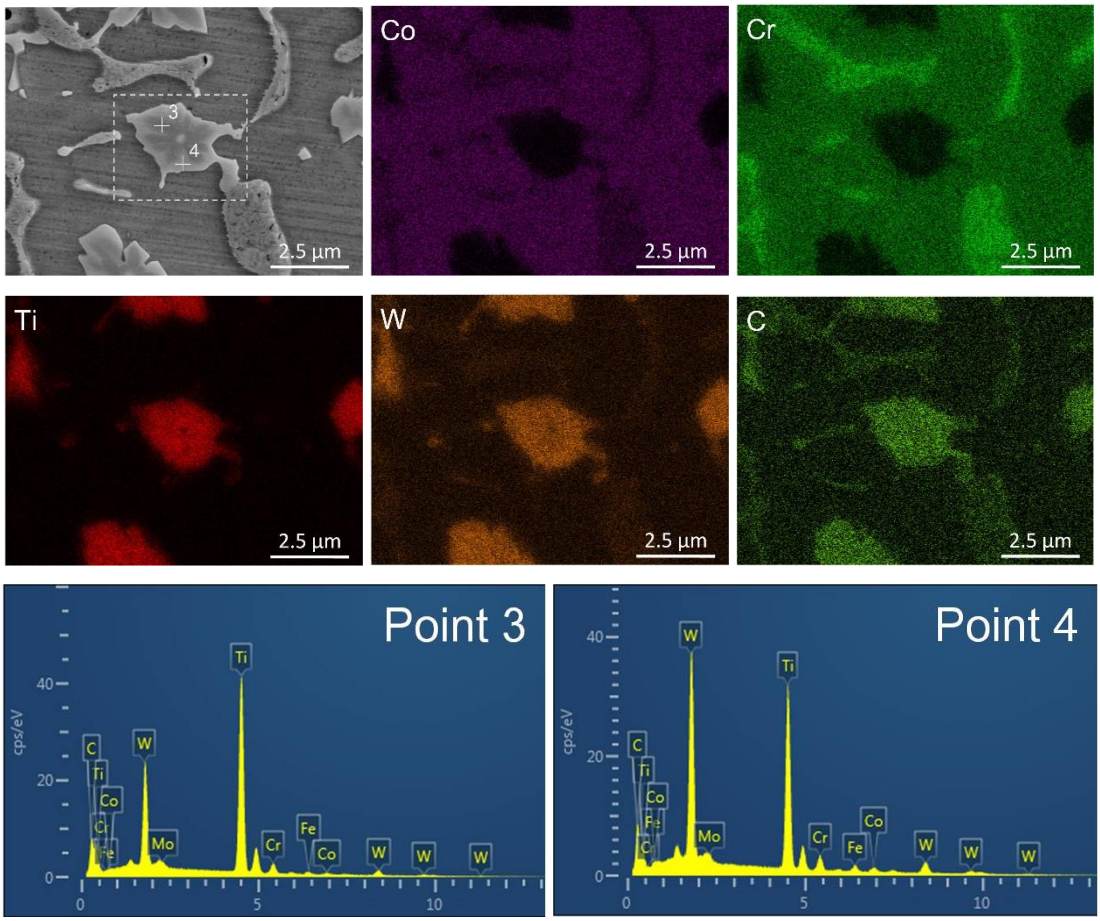

Figure 6. EDS analyses of the precipitated particles morphology and element distribution in TiC/Co-based composite coating containing CeO_2

Fig. 7 shows the EDS analyses of the square region in Fig. 6 under the high magnification scanning microscope. As shown in Fig.7, in the cladding layer with CeO_2 addition, the center of TiC and $TiWC_2$ particles is rich in Ce and O element, and the other areas of TiC and $TiWC_2$ particles mainly contain Ti element, W element and C element. It can be inferred that the core of TiC and $TiWC_2$ particles is Ce oxide. This indicates that Ce oxide can be used as a nucleation position for hard precipitates. Although aportion of CeO_2 decomposed during laser cladding, the rare earth Ce had strong chemical activity and appetency with O [24]. The newly formed or unmelted Ce oxide particles

in the coatings can act as heterogeneous nucleation sites in the melting pool because of their high melting point, and reduce the nucleation energy as well as improve the nucleation rate. At the same time, Ce element is beneficial to reduce the interfacial energy, surface tension and critical nucleation energy [25]. Therefore, an appropriate amount of CeO_2 addition will increase the formation of TiC and $TiWC_2$ precipitated particles and refine the particles size.

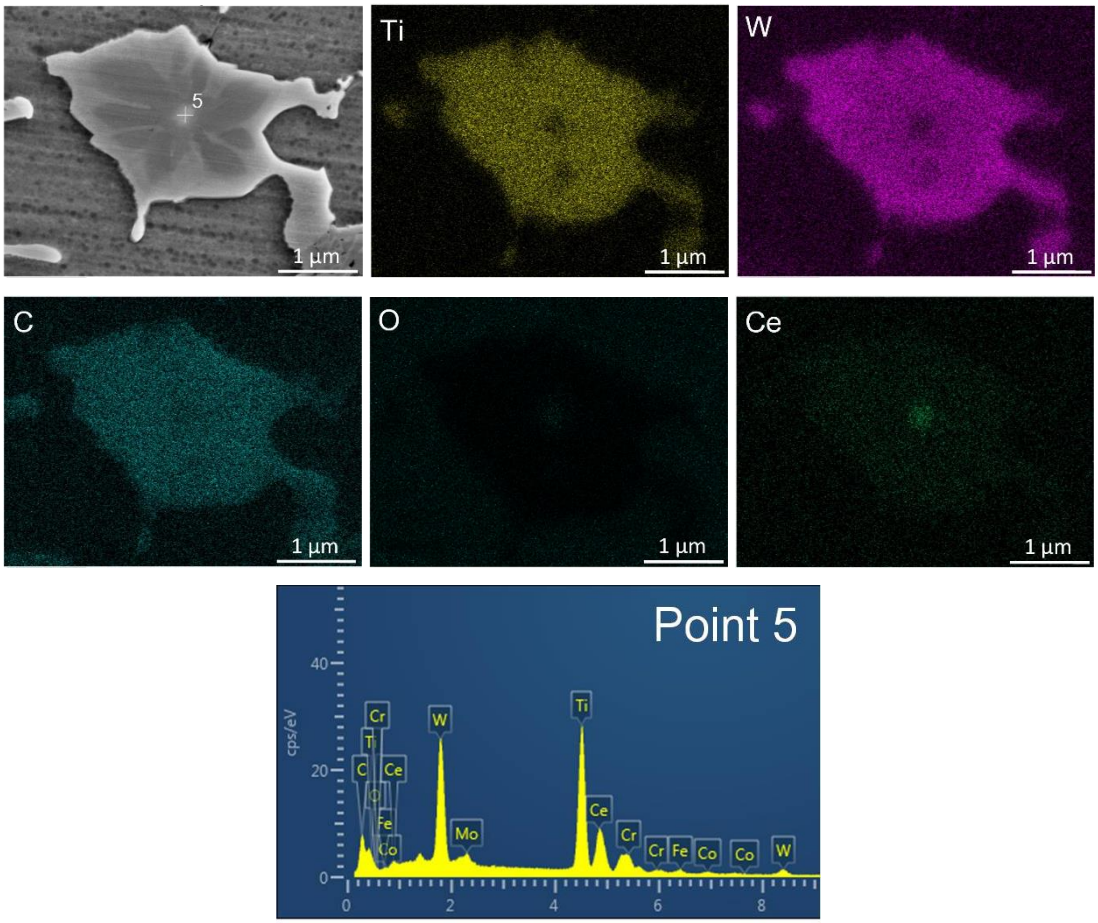

Figure 7. EDS analyses under the high magnification scanning microscope of the square region in Fig. 6

3.3 EIS results of TiC/Co-based composite coatings

Fig. 8 shows the impedance responses of TiC/Co-based composite coatings with different CeO_2 additions exposed to the 3.5 wt.% NaCl solution. Fig. 8(a) and Fig. 8(b) are the Nyquist plots and the Bode plots, respectively. As shown in Fig. 8(a), the Nyquist plots display the characteristic of depressed capacitive loops. The diameters of the capacitive loops are relatively similar. As shown in Fig. 8(b), the values of $|Z|_{f=0.01\ Hz}$ are also similar with magnitude of 10^4, indicating that with the CeO_2 addition of 0 wt.%, 0.5 wt.%, 1.5 wt.%, and 3 wt.%, the four TiC/Co-based composite coatings have excellent corrosion resistance. Furthermore, for all the coatings, the characteristic of two time constants can be recognized from the phase peaks as shown in the Bode plots.

Fig. 9 shows the equivalent circuit to extract the electrochemical parameters, R_s is the solution

resistance, $R_{o,\ film}$ is the resistance of the oxide film on coating surface, R_{ct} is the charge transfer resistance of the TiC/Co-based composite coating, $Q_{o,\ film}$ and Q_c are the constant phase elements corresponding to the $R_{o,\ film}$ and R_{ct} respectively [26]. The fitted results of parameters are displayed in Table 5.

As shown in Table 5, for the CeO_2 addition of 0 wt.%, 0.5 wt.%, 1.5 wt.%, and 3 wt.%, the values of $R_{o,\ film}$ are close to each other in a range of approximately 1000 $\Omega \cdot cm^2$, indicating a similar ability of generating oxide film on the coating surface. The value of R_{ct} increases as the CeO_2 addition increases from 0 wt.% to 1.5 wt.%, and then decreases. The largest R_{ct} appears at the CeO_2 addition of 1.5 wt.% (15.28 $k\Omega \cdot cm^2$). The order of R_{ct} for coatings with different CeO_2 additions is 1.5 wt.%>3 wt.%>0.5 wt.%>0 wt.%. The difficulty of charge migration in the coating is gradually reduced in the above order. The TiC/Co-based composite coating with 1.5 wt.% CeO_2 can hinder the charge migration most effectively, which is related to the high density TiC and $TiWC_2$ uniformly distributed on the coating surface. He et al. [27] reported that the particle size of TiC is small and the concentration is high, the corrosion resistance of the TiC/TiAl composite coating is relatively good. Thus, the TiC/Co-based composite coating with CeO_2 addition of 1.5 wt.% shows the most excellent corrosion resistance. The corrosion resistance decreases in the order of 1.5 wt.%>3 wt.%>0.5 wt.%>0 wt.%. This is also consistent with the findings of Zhang et al., namely, the appropriate addition of CeO_2 can improve the corrosion resistance of TiC-VC reinforced Fe based laser cladding layers, while excessive CeO_2 addition will lead to a decrease in corrosion resistance [28].

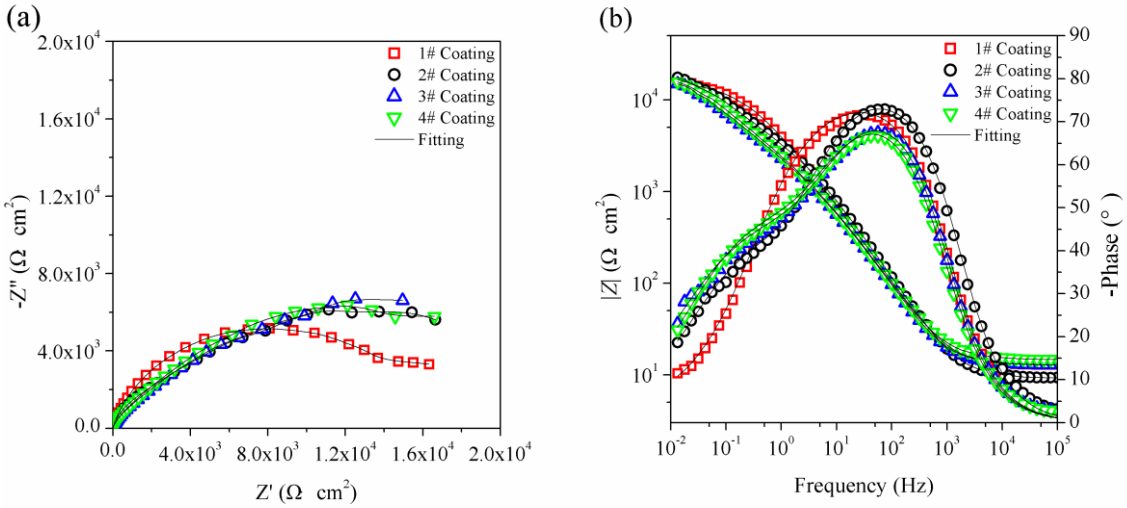

Figure 8. Electrochemical impedance spectra for TiC/Co-based composite coatings with CeO_2 additions of 0 wt.%, 0.5 wt.%, 1.5 wt.%, and 3 wt.% in the 3.5 wt.% NaCl solution. (a) Nyquist plot, (b) Bode plots

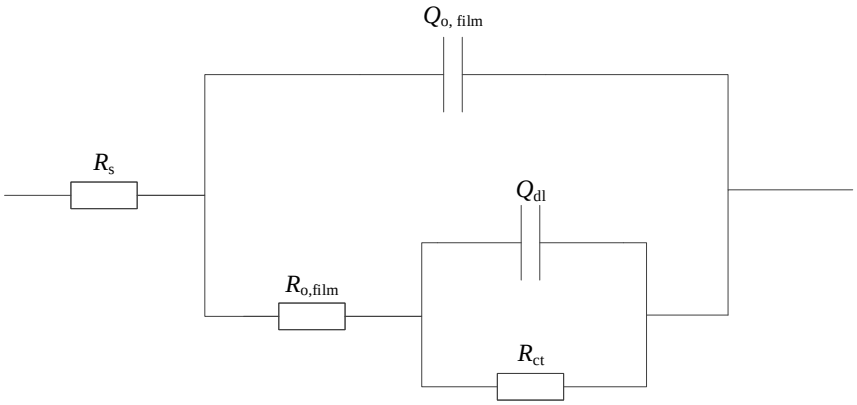

Figure 9. Equivalent circuit used for EIS fitting analysis

Table 5. Electrochemical impedance parameters for TiC/Co-based composite coatings with CeO_2 additions of 0 wt.%, 0.5 wt.%, 1.5 wt.%, and 3 wt.%

No.	Parameters							
	R_s ($\Omega \cdot cm^2$)	α_1	$Q_{o,\ film}$ ($\mu F \cdot cm^{-2}$)	$R_{o,\ film}$ ($k\Omega \cdot cm^2$)	α_2	Q_c ($\mu F \cdot cm^{-2}$)	R_{ct} ($k\Omega \cdot cm^2$)	Chi-square ($\times 10^{-3}$)
1#	8.3	0.86	60.7	2.02	0.37	78.3	11.11	0.348
2#	6.0	0.88	47.5	1.95	0.59	189.2	13.53	0.392
3#	8.2	0.86	67.9	1.03	0.56	223.6	15.28	0.382
4#	9.5	0.84	71.2	1.26	0.58	195.6	14.03	0.235

3.4 Hardness of TiC/Co-based composite coatings

Fig.10 shows the micro-hardness distribution of TiC/Co-based composite coatings with different CeO_2 additions. As shown in Fig. 10, the hardness of the cladding layer is extremely sensitive to the rare earth element content. As the rare earth element content increases, the hardness of the cladding layer gradually increases. When the cladding layer contained 0 wt.% CeO_2, the hardness value of the cladding layer was low, and the distribution was not smooth. The micro-hardness changes in the cladding layer are large, since the size and distribution of precipitated particles were extremely non-uniform. When the CeO_2 content was 1.5 wt.%, the hardness of the cladding layer was the highest, which is ascribed to thelargest number density of TiC and $TiWC_2$ precipitated particles. Yet the hardness of the cladding layer decreased when the CeO_2 content reached 3 wt.%. Under this condition, the TiC and $TiWC_2$ precipitated particles aggregated and the size distribution became uneven again compared to the cladding layer containing 1.5 wt.% CeO_2. Therefore, the morphology and distribution of TiC and $TiWC_2$ precipitated particles play a decisive role in the change of hardness of the cladding layer. The more uniform and fine the TiC and $TiWC_2$ precipitated particles are, the higher the hardness of the cladding layer will have. Other rare earth oxide has the analogous report. Li et al. [29] found that

adding Y_2O_3 can improve the hardness of laser cladded TiB/TiC-reinforced composite coatings, because the addition of Y_2O_3 improves the microstructural uniformity, and increases the volume fraction of TiC.

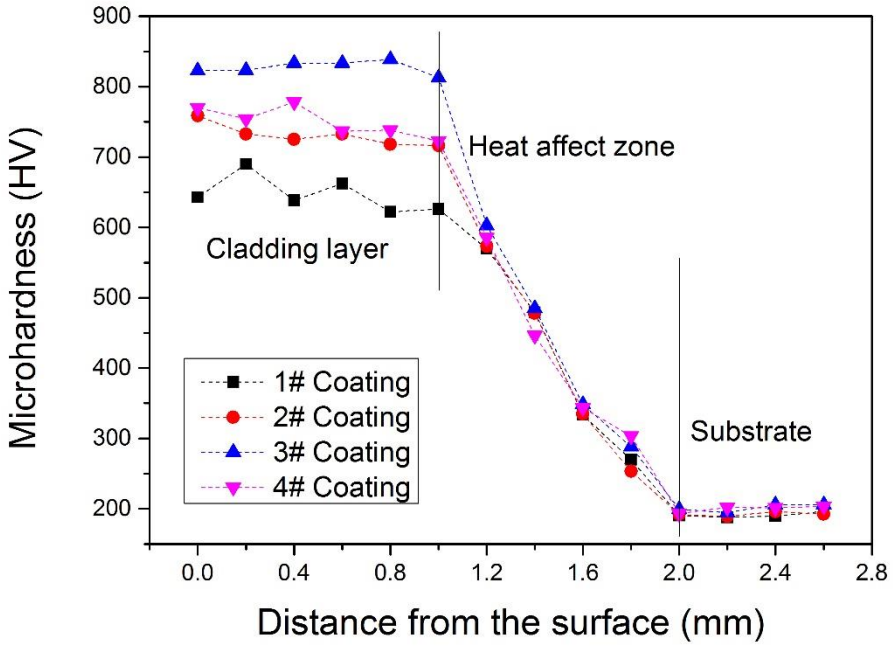

Figure 10. Micro-hardness distribution of the composite coatings with different CeO_2 contents

3.5 Wear resistance of TiC/Co-based composite coatings

It is well acknowledged that the wear resistance of the coating is largely determined by the microstructure and micro-hardness [30]. Especially the size and distribution of hard phase particles have a significant effect on the wear resistance of the coating [31]. Fig.11 shows the worn losses of laser cladded TiC/Co-based composite coatings with different CeO_2 contents. The wear volume can be determined through the following equation [32]:

$$V = \left[R^2 \arcsin\left(B/2R\right) - \left(B/2\right)\sqrt{R^2 - \left(B/2\right)^2} \right] L$$

where V is the wear volume, B is the width of specimens (mm), L is the width of wear track (mm) and R is the outer radius of wear ring (mm).

As shown in Fig.11, the wear volume and wear mass of cladding layer decrease firstly and then increase with the increase of CeO_2 contents. The cladding layer with 1.5 wt.% CeO_2 has the minimal wear losses, exhibiting the optimum wear resistance. However, the wear resistance decreases when the CeO_2 content reached 3 wt.%.

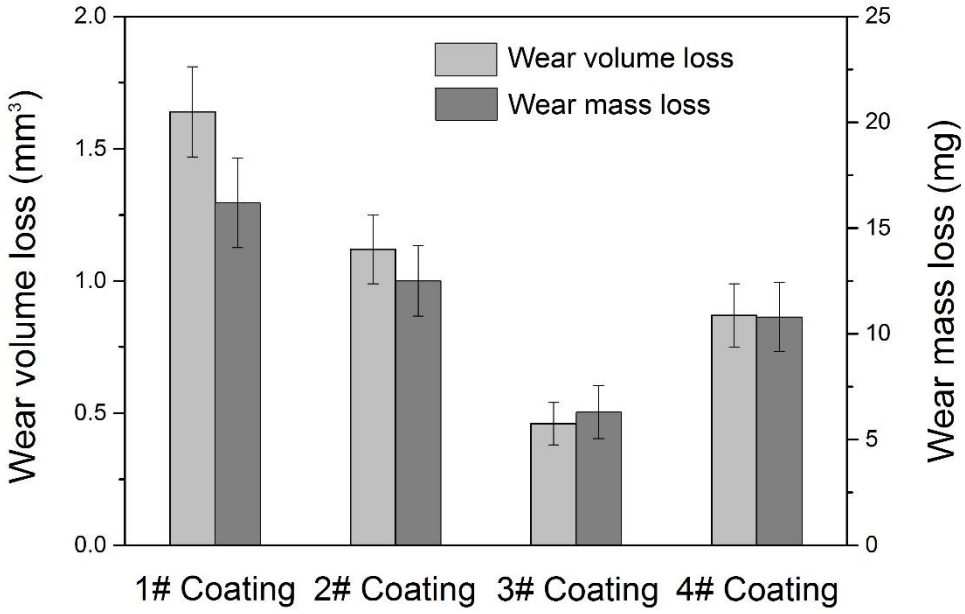

Figure 11. Wear losses of the composite coatings with different CeO_2 contents

Fig.12 shows the worn surfaces of laser cladded TiC/Co-based composite coatings with different CeO_2 additions. As shown in Fig. 12(a) and Fig. 12(b), there are a large amount of flaking and craters in the coating containing 0 wt.% CeO_2 after wear test, accompanied by deep ploughings. The main reason was the un-homogeneous size and distribution of TiC and $TiWC_2$ precipitated particles, which could lead to the grinding wheel micro-convex peak to come into contact with the matrix more easily, causing the wear of the coating. As the CeO_2 content increased to 0.5 wt.%, the coating wear zone became flat, and the particle flaking phenomenon and craters were reduced. No evidence for the flaking, and the ploughing was smaller and weakened when the CeO_2 content was 1.5 wt.% compared to other coating layers, as shown in Fig. 12(e) and Fig. 12(f). This is mainly because the dispersion strengthening effect from CeO_2 addition increased the hardness of the coating layer. The TiC and $TiWC_2$ particles distribution were more uniform, as shown in Fig. 4(e) and Fig. 4(f), and the depth of the grinding wheel micro-convex peak embedded in the coating was relatively reduced when wear test was carried out, so that the coating was more resistant to wear. When the CeO_2 content was 3 wt.%, a small amount of ploughing appeared on the surface of the worn sample, and there were a few craters on the worn surface due to material flaking, as shown in Fig. 12(g) and Fig. 12(h). This is due to the excess CeO_2 caused the aggregation and uneven distribution of TiC and $TiWC_2$ particles, and reduced the dispersion strengthening effect of TiC and $TiWC_2$ precipitated particles. Liu et al. [33] studied the effect of La_2O_3 on the wear resistance of laser cladded γ/Cr_7C_3/TiC composite coatings, and obtained similar results. Adding an appropriate amount (4 wt.%) of La_2O_3 can improve the wear of coatings, because the addition of La_2O_3 decreases the volume fraction of primary blocky Cr_7C_3 to Cr_7C_3/γ eutectics, however, excessive addition of La_2O_3 will deteriorate the wear resistance of the coating.

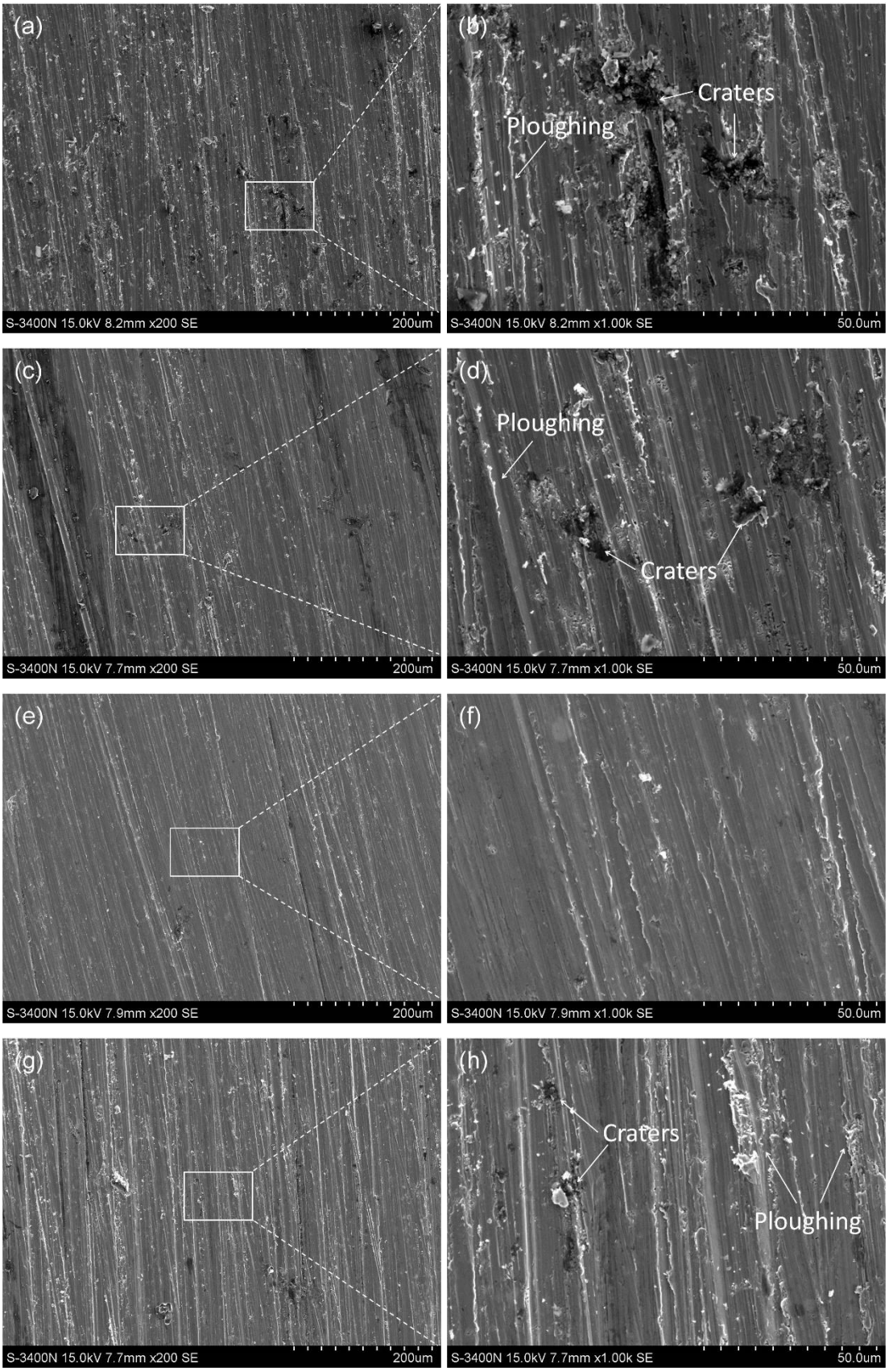

Figure 12. Worn surface morphology of the TiC/Co-based composite coatings: (a) and (b) 0 wt.% CeO_2, (c) and (d) 0.5 wt.% CeO_2, (e) and (f) 1.5 wt.% CeO_2, (g) and (h) 3 wt.% CeO_2

4. CONCLUSIONS

In this work, the laser cladded TiC reinforced Co-based coatings with different CeO_2 contents were successfully prepared. Effects of CeO_2 on microstructure, corrosion resistance, hardness, and tribological behavior of coatings have been studied. The following conclusions can be drawn:

(1) Small addition of CeO_2 would not affect the phase composition of TiC/Co-based composite coatings, and the coatings were composed of γ-Co, TiC, $TiWC_2$ and $Cr_{23}C_6$ phases.

(2) CeO_2 addition could change the morphology and distribution of TiC and $TiWC_2$ precipitated particles, the morphology of the TiC and $TiWC_2$ changes from dendrites to particles with the addition of CeO_2.

(3) Ce oxide can act as a nucleation position for hard precipitates, and appropriate CeO_2 addition could spheroidise and refine the TiC and $TiWC_2$ precipitated particles.

(4) The TiC/Co-based composite coating with the optimum addition of CeO_2 (1.5 wt.%) exhibits the most excellent corrosion resistance, micro-hardness, and wear resistance.

ACKNOWLEDGEMENTS
The work was financially supported by the Technique Support Program of State Administration for Market Regulation (No. 2019YJ005), and Science and Technology Program of Tianjin Administration for Market Regulation (No. 2019-W13 and 2018-W20).

References

1. J.L Liu, H.J Yu, C.Z Chen, F. Weng and J.J Dai, *Opt. Laser. Eng.*, 93 (2017) 195.
2. F. Weng, C.Z. Chen and H.J. Yu, *Mater. Design.* 58 (2014) 412.
3. H. Raghuram, C. Katsich, K. Pichelbauer, K. Koschatzky, C. Gachot and U. Cihak-Bayr, *Surf. Coat., Technol.* 377 (2019) 124897.
4. Y.B. Guo, Z.G. Li, C.W. Yao, K. Zhang, F.G. Lu, K. Feng, J. Huang, M. Wang and Y.X. Wu, *Mater. Design*, 63 (2014) 100.
5. D. Verdi, M.A. Garrido, C.J. Munez and P. Poza, *Mater. Sci. Eng. A,* 598 (2014) 15.
6. J. Zhao, Q.W. Gao, H.Q. Wang, F.Y. Shu, H.Y. Zhao, W.X. He and Z.S. Yu, *J. Alloys Compd.,* 785 (2019) 846.
7. J.D. Wang, L.Q. Li and W. Tao, *Opt. Laser Technol.,* 82 (2016)170.
8. S.T. Sun, H.G. Fu, X.L. Ping, X.Y. Guo, J. Lin, Y.P. Lei, W.B. Wu and J.X. Zhou, *Surf. Coat. Technol.,* 359 (2019) 300.
9. Y.N. Liu, R.L. Sun, W. Niu, T.G. Zhang and Y.W. Lei, *Opt. Laser Eng.,* 120 (2019) 84.
10. S.P. Sharma, D.K. Dwivedi and P.K. Jain, *Wear,* 267 (2009) 853.
11. L. Ding, S.S. Hu, *Surf. Coat. Technol.,* 276 (2015) 565.
12. X.X. Duan, S.Y. Gao, Q. Dong, Y.F. Zhou, M.Z. Xi, X.P. Xian and B. Wang, *Surf. Coat. Technol.,* 291 (2016) 230.
13. Z. Zhang, R. Kovacevic, *J. Manuf. Process.,* 38 (2019) 63.
14. L.Q. Li, J.D. Wang, P.P. Lin and H. Liu, *Ceram. Int.,* 43 (2017) 16638.
15. J.D. Wang, L.Q. Li, P.P. Lin and J.M. Wang, *Opt. Laser Technol.,* 105 (2018) 195.
16. F.Q. Li, Z.Z. Gao, L.Q. Li and Y.B. Chen, *Opt. Laser Technol.,* 77 (2016) 134.
17. M.M. Savalani, C.C. Ng, Q.H. Li and H.C. Man, *Appl. Surf. Sci.,* 258 (2012) 3173.
18. Y.C. Cai, Z. Luo, M.N. Feng, Z.M. Liu, Z.Y. Huang and Y.D. Zeng, *Surf. Coat. Technol.,* 291 (2016)

222.
19. Y. Fan, G. Jin, X.F. Cui, Y. Li and Z.H. Gao, *Surf. Coat. Technol.*, 288 (2016) 25.
20. L. Ding, S.S Hu, X.M Quan and J.Q. Shen, *J. Alloys Compd.*, 659 (2016) 8.
21. Y.C. Cai, Z. Luo and Y. Chen, *High Temp. Mater. Proc.*, 37 (2017) 209.
22. Y.C. Cai, Z. Luo, Y. Chen and S.S. Ao, *Surf. Eng.*, 33(2017) 936.
23. Q.T. Li, Y.P. Lei and H.G. Fu, *Appl. Surf. Sci.*, 316 (2014) 610.
24. M.X. Li, S.H. Zhang, H.S. Li, Y.Z. He, J.H. Yoon and T.Y. Cho, *J. Mater. Process. Technol.*, 202 (2008) 107.
25. Y.S. Tian, C.Z. Chen, L.X. Chen and Q.H. Huo, *Scripta Mater.*, 54 (2006) 847.
26. G.L. Hou, Y. Ren, X.L. Zhang, F.X. Dong, Y.L. An, X.Q. Zhao, H.D. Zhou and J.M. Chen, *Ultrason. Sonochem.*, 60 (2020) 104799.
27. X. He, R.G. Song and D.J. Kong, *Opt. Laser Technol.*, 112 (2019)339.
28. H. Zhang, Y. Zhou, Z. Zou and C. Shi, *J. Rare. Earth.*, 32 (2014) 1095.
29. J. Li, X. Luo and G.J. Li, *Wear*, 310 (2014) 72.
30. L. Ding, S.S. Hu, X.M. Quan and J.Q. Shen, *J. Mater. Process. Technol.*, 252 (2018) 711.
31. Z.F. Chen, H. Yan, P.L. Zhang, Z.S. Yu, Q.H. Lu and J.L. Guo, *Surf. Coat. Technol.*, 372 (2019) 218.
32. H. Tan, Z. Luo, Y. Li, F. Yan and R. Duan, *Opt. Laser Technol.*, 68 (2015) 11.
33. X. Liu, R. Yu, *Mater. Chem. Phys.*, 101 (2007) 448.